This is a repository copy of *Spin echo small angle neutron scattering using a continuously pumped He-3 neutron polarisation analyser*.

White Rose Research Online URL for this paper:
http://eprints.whiterose.ac.uk/85681/

Version: Accepted Version

Article:

Spin Echo Small Angle Neutron Scattering (SESANS) using a continuously pumped ^{3}He neutron polarisation analyser

S.R.Parnell,[1] A.L.Washington,[1, 2] K.Li,[1] H.Yan,[1] P.Stonaha,[1] F.Li,[1] T.Wang,[1] A.Walsh,[3] W.C.Chen,[4, 5] A.J.Parnell,[6] J.P.A.Fairclough,[2] D.V.Baxter,[1] W.M.Snow,[1] and R.Pynn[1, 7]

[1]*Centre for Exploration of Energy and Matter, Indiana University, Bloomington, Indiana, USA, 47408*
[2]*Department of Mechanical Engineering, The University of Sheffield, Sheffield, UK, S1 3DJ*
[3]*Department of Chemistry, The University of Sheffield, Sheffield, UK, S3 7HF*
[4]*National Institute of Standards and Technology, Gaithersburg, Maryland, USA, 20899*
[5]*University of Maryland, College Park, Maryland, USA, 20742*
[6]*Department of Physics and Astronomy, The University of Sheffield, Sheffield, UK, S3 7RH*
[7]*Neutron Sciences Directorate, Oak Ridge National Laboratory, Oak Ridge, USA, 37831*
(Dated: October 23, 2014)

We present a new instrument for spin echo small angle neutron scattering (SESANS) developed at the Low Energy Neutron Source (LENS) at Indiana University. A description of the various instrument components is given along with the performance of these components. At the heart of the instrument are a series of resistive coils to encode the neutron trajectory into the neutron polarisation. These are shown to work well over a broad wavelength range of neutron wavelengths. Neutron polarisation analysis is accomplished using a continuously-operating neutron spin filter polarised by Rb-spin exchange optical pumping of ^{3}He. We describe the performance of the analyser along with a study of the ^{3}He polarisation stability and its implications for SESANS measurements. Scattering from silica Stöber particles is investigated and agrees with samples run on similar instruments.

Keywords: Helium-3, hyperpolarised, SESANS, optical pumping, laser, spin filter, spin echo

INTRODUCTION

Liouville's theorem has always been a limiting factor in neutron scattering measurements. Any attempt to focus a neutron beam onto a sample will result in increased beam divergence and consequently decreased resolution of the momentum transfer. In traditional elastic neutron scattering experiments, measuring small scattering angles, and, hence, large length scales, requires limiting the angular divergence of the neutron beam and losing much of the neutron flux. To escape this limitation, the Spin Echo Scattering Angle Measurement (SESAME) technique encodes the scattering signal into the polarisation of a beam of neutrons [1–3]. This eliminates, to a large extent, the coupling between beam collimation and momentum resolution, allowing for measurements of large scattering objects (10-1000's nm) without unacceptable losses of neutron flux. The SESAME technique for studying large scale structures has been implemented at a number of facilities with the development of several new instruments [4–6]. In this paper, we explore this option in terms of practical performance details and implementation along with experimental results.

We have developed a multipurpose SESAME instrument [7] for both transmission and reflection measurements. In transmission, the technique is referred to as Spin Echo Small Angle Neutron Scattering (SESANS) [2, 8] while in reflection it is called Spin Echo Reflection Grazing Incidence Scattering (SERGIS)[9, 10]. The SESAME beamline has been installed at the pulsed 13 MeV Low Energy Neutron Source at Indiana University [11, 12]. This paper focuses purely on the SESANS technique, however with additional motor control this instrument can be used in reflection geometry for SERGIS or diffraction geometry for Larmor diffraction.

The SESANS technique uses a neutron beam initially polarised in the $| + y >$ direction (see figure 1 for the coordinate system). The beam first passes through an abrupt, 90° change in the magnetic field direction, which splits the neutron beam into two in-phase wave states with opposite spins i.e. $| + z >$ and $| - z >$. These wave states then enter triangular magnetic prisms with magnetic fields in each of the triangular regions, alternately arranged along the $+z$ and $-z$ directions, as shown in Figure 1. Since the total energy of each neutron is conserved, the neutron velocity depends on the Zeeman interaction with the surrounding magnetic field, and the two spin states refract in different directions when they pass through the inclined boundary between each triangular region of the prism. A second triangular prism, with opposite fields to the first, returns the neutron waves to being parallel, yet spatially separated by a distance of the order of a few hundred nanometers, known as the spin echo length (Z) (see figure 1). A secondary spectrometer, located after the scattering sample, recombines the two neutron spin states, leading to a spin echo. Any scattering from a sample will result in a relative phase between the two spin states at the end of the instrument, and the initial (instrumental) polarisation will not be retrieved; i.e. the echo signal will be diminished. In this geometry, the Larmor phase of a scattered neutron is linearly proportional to its scattering angle. The Larmor phase is manifested in a change in polarisation which occurs due to the difference in phase for the two spin states. As a

result, the polarisation of the neutron beam is the cosine Fourier transform of the entire scattering signal, allowing SESANS to determine the scattering via measurement of the final beam polarisation [13].
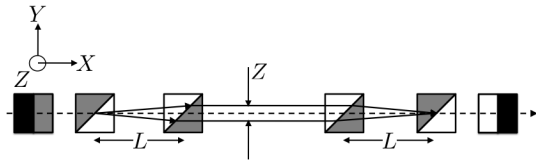

Figure 1. The arrangement of magnetic triangular prisms for SESAME. Unshaded triangles contain uniform magnetic fields along the -z axis, shaded triangles have fields along +z axis, whilst the solid black regions have field along the y axis. Rays associated with waves representing the two neutron spin states are shown and Z is the spin echo length. The path of the neutron beam is indicated by the dashed line.

The accessible spin-echo length for a neutron of wavelength λ for our setup utilising a series of resistive prisms is given by equation 1;

$$Z = cBL\lambda^2 cot\theta \qquad (1)$$

where c=$1.476\times10^{14}T^{-1}m^{-2}$, L is the separation between the prisms (as shown in figure 1) and θ is the angle between the hypotenuse of the prism and the beam direction (x in figure 1). Therefore in any time of flight experiment in which multiple wavelengths are used, a range of spin echo length is probed simultaneously. In time of flight measurements the extent of this range is usually chosen by selecting a particular static magnetic field strength (B).

For details of interpreting SESANS data the reader is directed to a recent work in reference [14]. Certain omissions in this work are addressed in recent work from our group [15], which presents the theory in terms of conventional notation used for Small Angle Neutron Scattering (SANS). Briefly, the salient points are summarised below. For any SESANS measurement the quantity measured is given by;

$$P(z) = \exp(\Sigma_t[G(z) - 1]) \qquad (2)$$

where P(z) is the echo polarisation due to the scattering obtained by measuring the polarisation with the sample in (P_s) and corrected for the instrumental polarisation (P_0) i.e. ($P(z) = P_s/P_0$) and Σ_t is the fraction of neutrons that are scattered *once* by a sample of thickness t. G(z) is related to the Debye autocorrelation function $\gamma(r)$

To practically determine G(z) a series of measurements are made of the spin echo polarisation with and without the sample. It is also important to note that the SESANS technique allows the measurement of the total scattering in absolute terms, as shown by equation 2 since G(z) $\rightarrow$ 0 as z $\rightarrow \infty$.

As shown in reference [15] the total coherent neutron scattering scales with the neutron wavelength squared and linearly with the sample thickness then a plot of $1/\lambda^2 ln(P_s(z)/P_0(z))$ should reach a constant value at large z as G(z) tends to zero at large z. This quantity has been recently termed 'the normalised SESANS signal'. Therefore from equation 2 both G(z) and Σ_t can be determined. The normalised SESANS signal also allows comparisons between different neutron scattering instruments and spin echo lengths as the dependence upon the neutron wavelength λ and magnetic field B can be corrected for allowing several different measurements at different wavelengths and magnetic fields to be collapsed into one dataset.

SESANS instruments are now being developed at a number of beamlines, at both reactor sources, for example at TU Delft [6], and pulsed sources, such as the instruments OffSpec [4, 5] and Asterix [16]. To date, and as far as we are aware, these have all utilised supermirror analysers. In this work, we report our experience of operating a ^{3}He based device as a polarisation analyser. We report the basic instrument configuration, performance of the various components and some recent results on silica Stöber particles. Considerable focus is given to the ^{3}He neutron spin filter as this is, to our knowledge, the first time that such a device has been used for SESANS. The appendices describe the effect of the stability of the ^{3}He polarisation on the measured G(z) and also the algorithm used to stabilise the ^{3}He polarisation.

INSTRUMENT DESCRIPTION

The SESAME beamline at the Low Energy Neutron Source (LENS) [11, 12] is first and foremost a time-of-flight polarised neutron instrument with usable wavelength neutrons from 2.5 Å to 11 Å. The instrument is used for SESANS and also the development of polarised neutron instrumentation [17–20]. The neutrons are produced at a repetition rate of 20 Hz, are thermalized within a 15 cm diameter water reflector, and cooled with a 10 mm thick methane moderator at T≈6 K. The neutrons are transported from the moderator via supermirror guides. Direct line-of-sight from the SESAME flight-path to the source is prevented through the use of a polarizing bender. NiTi supermirror guides are then used to transport the polarised beam to the instrument.

The beam passes through a series of resistive coils, which provide the necessary spin manipulation to encode the scattering. The coils are π flippers, $\frac{\pi}{2}$ flippers and prisms. The $\frac{\pi}{2}$ flippers stop and start the precession; a π flipper at the centre of the precession region flips the neutron spins; whilst four prism coils with inclined current sheets serve to encode the scattering angle [21]. There are two prism coils placed before the sample and two after. The polarisation of the scattered neutrons is anal-

ysed using a ^{3}He neutron spin-filter. This continuously operating ^{3}He neutron spin filter uses alkali (Rb) metal Spin-Exchange Optical Pumping (SEOP) [22]. Since a ^{3}He spin filter is based on spin dependent absorption of neutrons, it decouples the spin state selection from the neutron optics and has a higher angular acceptance than typical super mirrors [23]. Turning off the SEOP laser during data collection results in a loss of ^{3}He nuclear polarisation, with a time constant $T_1 \approx 17$ hours ($P_{He}(t) \propto \exp(-t/T_1)$). The change of ^{3}He polarisation in turn effects the performance of the beamline as a whole, as the device has a time dependent analysing power. This can be overcome by continuously pumping during measurements [24–26]. Finally, the scattered beam is detected using an array of 1/2" diameter 1-D position sensitive ^{3}He detector tubes.

Optics

A 40 mm long solid-state polarising bender is used to polarise the incident beam. The bender serves a dual purpose: (1) it produces a polarised incident beam and (2) fast neutrons cannot propagate through the guide system along any straight line path. The bender is made from a stack of 170 curved silicon wafers each 150 μm thick. On the concave side of each wafer is an m=3 polarising supermirror composed of layers of $Fe_{89}Co_{11}$ and Si, followed by Gd/Si antireflecting layers and an absorbing layer of Gd. On the convex side is an m=2 polarising supermirror composed of layers of Fe and Si and the same antireflecting and absorbing layers [**?**].

The supermirror guides, manufactured by Osmic have internal dimensions of 25×75 mm^2. Guides upstream from the bender are angled 1.5° above the horizontal, whilst guides after the bender are horizontal. The NiTi coatings are m=3 and m=2 on the 25 mm and 75 mm faces, respectively. Tests were carried out on the POSY-I reflectometer at IPNS on a short 185 mm guide section with magnetic fields of 16, 45 and 300 G applied using permanent ceramic magnets. The loss in neutron polarisation was acceptably low (less than 2% per bounce) with ceramic magnets producing a 300 G field perpendicular to the m=3 faces.

Spin manipulation coils

The various spin manipulation devices throughout the SESAME beamline are all made of pairs of adjacent solenoids that are wound with aluminium wire, which has low neutron absorption. The aluminium wire is coated in an insulating layer of low neutron scattering cross section. Measurements of this wire show a transmission of 97.5%/layer. To increase transmission and prevent neutron depolarisation due to uncontrolled field transitions

[21], the wires of the upstream and downstream faces of each device are folded away from the beam. The various types of coils are shown along with the magnetic field orientations in figure 2. Electromagnetic guide fields are installed between each pair of prisms to preserve the polarisation and extend the accessible spin echo length of the instrument by increasing L in equation 1. The last coil before the $\frac{\pi}{2}$ flip is used to correct for any imbalance in the total field integral. This is done by scanning the current and setting it to achieve the maximum echo polarisation.
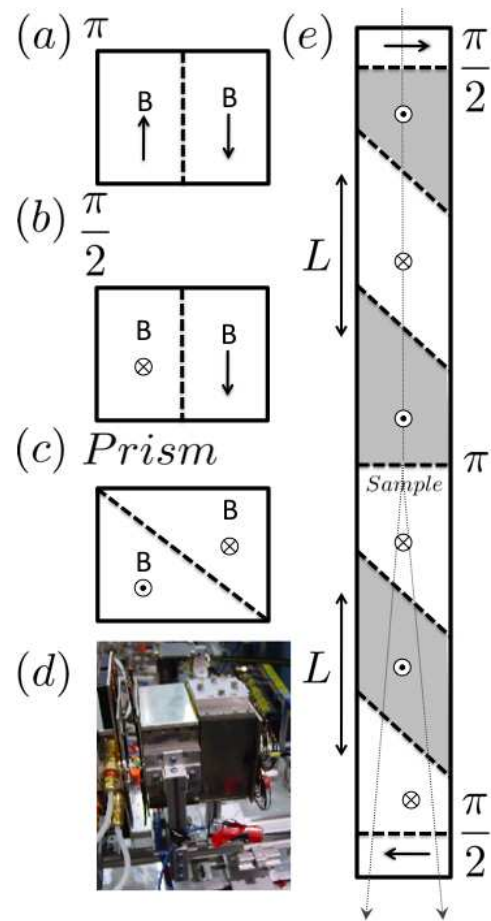

Figure 2. Schematics of the various coils used for spin encoding. (a) is a π flipper, (b) a $\frac{\pi}{2}$ flipper and (c) a Prism. The dotted line indicates the location of the current sheet interface in each device. (d) is a picture of a $\frac{\pi}{2}$ coil and (e) is a schematic showing the total magnetic field arrangement along the beam line. The regions between the $\pi/2$ flippers on either half of the instrument in part (e) of the figure are filled with magnetic fields along the $+z$ and $-z$ axes (i.e. into and out of the plane of the page). Before the first $\frac{\pi}{2}$ and after the last $\frac{\pi}{2}$ the magnetic fields are in the plane of the page. The neutron beam is shown as a dashed line.

The solenoids from which the magnetic prisms are constructed have been discussed at length in a number of publications [27, 28]. Each coil is individually powered

by a Kepco BOP 20-20M bipolar power supply operating in constant current mode. The output current is controlled via a computer through a National Instruments DAC card. Each coil has a resistance of 1.1 Ω. Field mapping has shown that the prisms produce 8.89 G A^{-1} near the hypotenuse. This is the magnetic field value which corresponds to B in equation 1. Care was taken to limit the power supply fluctuations including drift and noise. Typically these are at the level of 0.02% as monitored over a 24 hour period using a commercial Direct Current-Current Transformer (DCCT). To prevent the solenoids from overheating, each triangular frame is water-cooled and air-cooled allowing up to 15A to be applied.

The two π flippers are constructed in a manner similar to the prisms, but with a different cross sectional shape (the flipping plane is perpendicular to the neutron beam) and without water cooling. The same aluminium wire is used.

All solenoids used in the π and $\frac{\pi}{2}$ have a height (parallel to the field direction) of 140 mm, a width of 70 mm, and extend 70 mm along the neutron beamline. They are yoked in 1.5 mm thick mumetal. All the flipping in these coils occurs at the current sheet interface and, since there is no attempt to rotate the neutrons' spins using Larmor precession, these flippers work for any neutron wavelength and do not require ramping of the applied current.

Detectors

At the exit of the final neutron guide is a low efficiency (0.5%) ^{3}He neutron monitor. The active area of the monitor is 75.0 mm × 25.4 mm and thus covers the entire guide exit. The primary detector used is an array of sixteen 12.7 mm diameter position sensitive ^{3}He filled tubes as shown in figure 3, arranged in two rows of eight, one behind the other and offset from on another such that the detector efficiency is almost constant perpendicular to the axis of the tubes except for a series of narrow gaps. The gas in the tubes is at 10 bar and each tube has an efficiency of neutron capture >90% calculated for 5 Å neutrons. Each tube has ≈2 mm resolution along the tube length.

^{3}He Analyser

The ^{3}He cell (Mars) was fabricated at NIST using the procedure outlined in [29]. The cell body is made from Corning 1720 with optically flat windows made from re-blown GE180 alumina silicate glass. The flat windows are intended to reduce any lensing and birefringent effects which can occur in cells from re-blown glass. This is critical in our application as the cell cannot be side pumped as in similar online pumping experiments [25].
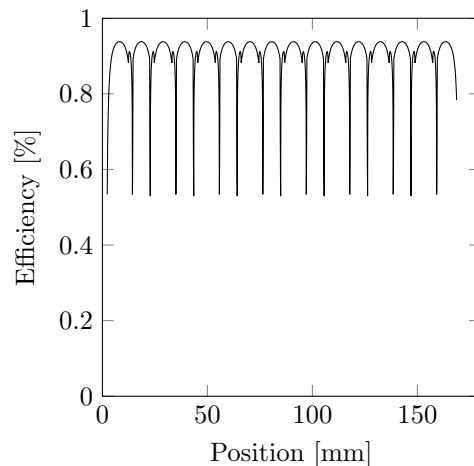

Figure 3. Detector efficiency calculated at λ= 4.05Å across the detector tubes.

The windows are 8 mm thick and the cell body is 80 mm long with an inner diameter of 60 mm. The cell pressure measured by neutron transmission at NIST is 0.9 Bar [29, 30]. The flat windows provide a uniform analysing path for the scattered beam because they provide for a uniform path length through the cell, compared to re-blown cells. However due to our instrumental geometry there are still differences between going through the center of the cell and across the cell. These result in a difference of < 1 % in analysing power for wavelengths > 2.5 Å over the whole cell [31] .

The ^{3}He cell is pumped by a Oclaro comet laser system with a fibre-coupled ∼30 W CW laser. The spectrum of the laser is narrowed down to 0.24 nm by a Volume Bragg Grating (VBG). The peak wavelength can be tuned to the Rb D$_1$ transition line mainly by adjusting the laser drive current at the fixed temperature of 19.89 °C. The spatial profile of the laser is homogenised using a fibre and the polarisation of the laser emission is separated by a polarising beam cube at the output of the fibre (see Figure 4 (a)). This splits the beam into two components in approximately a 2:1 ratio (which is due to the polarisation preserving fibre) and the higher power beam is incident on the front of the cell whilst the second lower power beam (with opposite helicity) is used to illuminate the rear of the cell. The laser light is brought parallel to the ^{3}He holding magnetic field using mirrors fabricated from single crystal silicon. Fused silica windows with total thickness of 4 mm are used to enclose the cell inside the oven.

The ^{3}He cell is held in a shielded solenoid which contains Nuclear Magnetic Resonance (NMR), Electron Paramagnetic Resonance (EPR) and Adiabatic Fast Passage (AFP) coils as shown in figure 4 (a). The AFP coil is a sine coil close to the solenoid winding and is not shown on the figure. During the course of the measurements
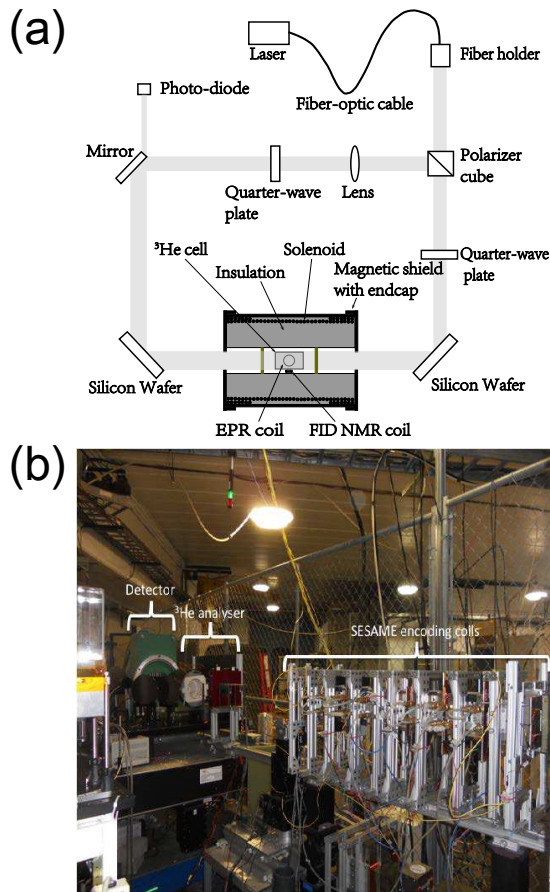
Figure 4. (a) Schematic of the continuously pumped ^{3}He analyser. Neutron beam (not shown) passes right to left through the dielectric mirrors. The oven is omitted for clarity. (b) Picture of the device installed on the SESAME beamline at LENS, showing SESAME encoding coils, ^{3}He analyser and detector.

the absolute polarisation of the ^{3}He is measured using the change in the EPR resonance of the Rb frequency [32]. This frequency is monitored via the peak of fluorescence of the D_2 emission using photodiodes whilst the ^{3}He polarisation is reversed using an in-built coil via a frequency swept AFP pulse similar to [33] with losses of typically of 0.1% per flip. This could be improved by implementing a Gaussian envelope on the sweep function [34, 35]. A Free Induction Decay (FID) NMR system similar to that described in [36] is also used to monitor the relative polarisation of the ^{3}He. Using FID NMR, a cell lifetime (T_1) of 107 $\pm$2 hours was measured offline. No attempt was made to measure the orientational dependence of the ^{3}He lifetimes (T_1) [37].
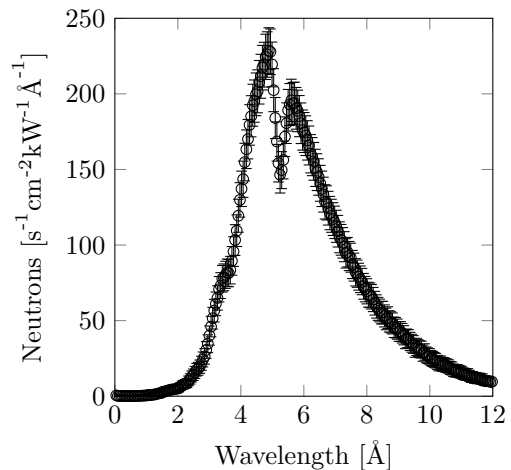

Figure 5. Polarised neutron flux at the sample position as a function of neutron wavelength. Integrated flux from 3-12 Å is 2430 neutrons s^{-1} cm^{-2} at a typical power of 3kW.

PERFORMANCE

Neutron Flux

The flux was measured using a high efficiency ($\approx$ 100%) ^{3}He pencil detector, measuring 100 mm wide $\times$ 25 mm tall and mounted at the sample position with the polariser in position. A thin slit was used to define the beam area and to ensure that the beam was incident on the centre of the detector. The spectrum is hown in figure 5, the dip observed in the spectrum at 5.06 Å is a result of diffraction from the {111} plane of Si in the bender. Similar dependence has been reported for previous solid-state benders [38] and can be avoided by more careful design. The total neutron flux at the sample position integrated over the wavelength range from 3-12 Å was 810 neutrons cm^{-2}s^{-1}kW^{-1}. The typical proton beam power for the LENS neutron source is 3kW.

Polariser and analyser efficiency

To check the instrument performance and alignment of the bender, the polarisation was measured with only guide field between the bender and analyser. Flipping of the ^{3}He allows the measurement of the polariser and analyser ($P_A \times P_B$) efficiency [39]. The efficiency (P_A) of the analyser is given by;

$$P_A(\lambda) = tanh(P_{He}\mathcal{O}_{He}(\lambda)) \tag{3}$$

where $\mathcal{O}_{He}(\lambda) = 7.33\times10^{-2} \times pl\lambda$ and P_{He} is the ^{3}He nuclear polarisation. Using EPR to measure the ^{3}He polarisation and with pl=7.2 $Bar\cdot$ cm, determined from neu-
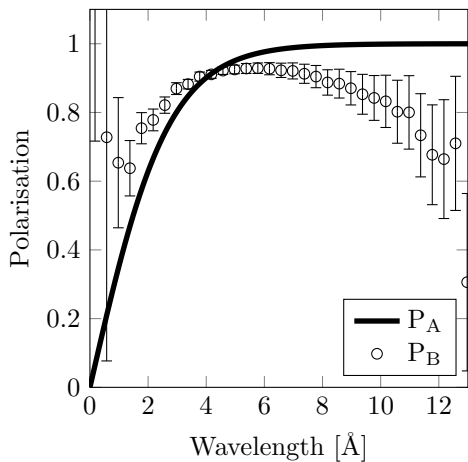
Figure 6. Bender efficiency (P_B) extracted by using the ^{3}He analyser as a flipper along with the calculated ^{3}He analyser efficiency (P_A) as a function of neutron wavelength.
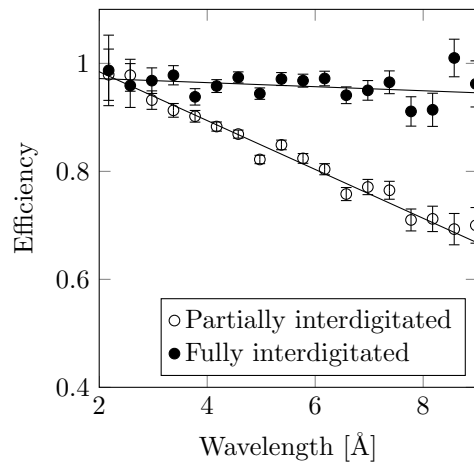

Figure 7. Comparison of the flipping efficiency of two different prism coils operating at 15 A. The wires at the hypotenuse are fully interdigitated in one coil and partially in the second. The lines are a guide to the eye.

tron transmission, all quantities in equation 3 are known and the performance of the bender can be extracted (see figure 6).

The bender efficiency peaks at 4-6 Å, falling off at higher wavelengths agreeing with earlier measurements [?]. This is well matched to the flux profile as shown in figure 5. It may be possible to extend this range by adding in a second polariser using either a combination of reflection and transmission polarisers or a single-bounce polariser followed by a ^{3}He cell as shown by Dalgliesh *et al.* [40].

Spin encoding coil performance

In order to maximise the instrumental polarisation (P_0), the losses due to the Larmor encoding coils must be minimised. In earlier work it was shown how symmetry across the various components serves to cancel out most of the magnetic field aberrations [21, 28, 41]. Despite this symmetry allowing most aberrations to be cancelled, the total polarisation can still be low due to low flipping efficiency at the various current sheet interfaces between field regions [19].

Simulations using finite element methods and a Bloch equation solver [42] show that the majority of this depolarisation comes from the use of round wire at the interface between the two triangular solenoids that form the prism. Interdigitatation of the wires belonging to neighbouring current sheets should significantly improve the performance [19]. The simulations also show that the degree of depolarisation increases with the coil current density. This effect is not strong in the π-flipper as this is operated at relatively low currents of 3-5A. However in order to reach long spin-echo lengths, it is important to achieve a high magnetic field (B) in the prisms. Hence de-

polarisation at interfaces becomes a non-trivial loss effect which must be minimised. This is shown clearly in figure 7 which shows a comparison of the flipping efficiency of two prism coils. In these measurements the devices were tested as a simple π flipper energised at 15 A. Physical inspection of the coils used in figure 7 shows that one has close to perfect inter-digitation at the current sheet interfaces whilst the second has gaps. The prism with gaps has a lower overall efficiency at the high current. Further examination of the spatial dependence of the efficiency shows that the efficiency varies with position and that this spatial dependence corresponds to the regions where the inter-digitation of the wires has failed. The prism with good inter-digitation has no corresponding spatial dependence in its flipping efficiency.

Measurements of the neutron wavelength dependence of the prism efficiencies were made at applied currents of 5A and were above 90% even at 10Å. These were performed using them in a π flipping mode. Using these measurements for the four prisms and the measured efficiencies of the π and $\frac{\pi}{2}$ flippers the expected echo polarisation is calculated. A comparison between the calculated echo, measured echo and instrumental polarisation is shown in figure 8. This shows that at short wavelengths the full instrumental polarisation is recovered in spin echo. However at longer wavelength, additional depolarisation is observed due to Larmor aberrations. Moreover this suggests that improvements in the flipping efficiency would allow a significant increase in echo polarisation. Such improvements may be possible using a new superconducting Wollaston prism that is under development [20], although this would still not recover the total instrumental polarisation based upon the calculated values.
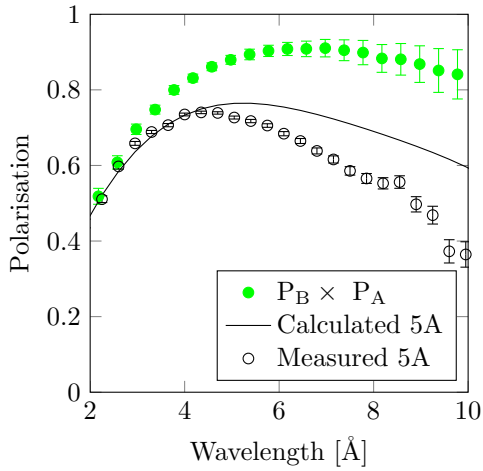
Figure 8. Instrumental polarisation ($P_A \times P_B$), calculated echo polarisation using the experimentally determined coil efficiencies and measured echo polarisation.

Stability of ^{3}He polarisation

The saturated ^{3}He polarisation was monitored by EPR during the course of several cycles of experiments. The uncertainty on each point comes from the fitting of the EPR signal. During the first two cycles of operation (Cycle 1 and Cycle 2), a variation of the ^{3}He polarisation of 3.0% and 3.3% was observed. There was also a difference in average polarisation between the two cycles which was due to realignment of the laser to better illuminate the cell. Any variation in P_{He} will change the total analysing power of the instrument according to equation 3 and hence should be minimised. For a detailed discussion see appendix 1.

The main source of fluctuations in the device was the optical pumping laser since the laser wavelength drifts with time, over the course of several hours (Appendix figure 12). To solve this, a feedback mechanism was implemented to change the laser current to tune the laser back onto resonance. The details of the feedback loop are discussed in the appendix. Once this feedback was implemented variations in the ^{3}He polarisation of 2.3% and 1.8% were observed during cycles 3 and 4. The effect of the ^3He polarisation drift at this level is to render measurements below 2.5 Å unreliable as the drift in the analyser efficiency at these wavelengths is large. However above 2.5 Å fluctuations in the ^3He polarisation of 2% represents a total possible contribution to the accuracy of $< 1\%$ of the determined SESANS signal P_s/P_0. For most SESANS measurements this is acceptable.
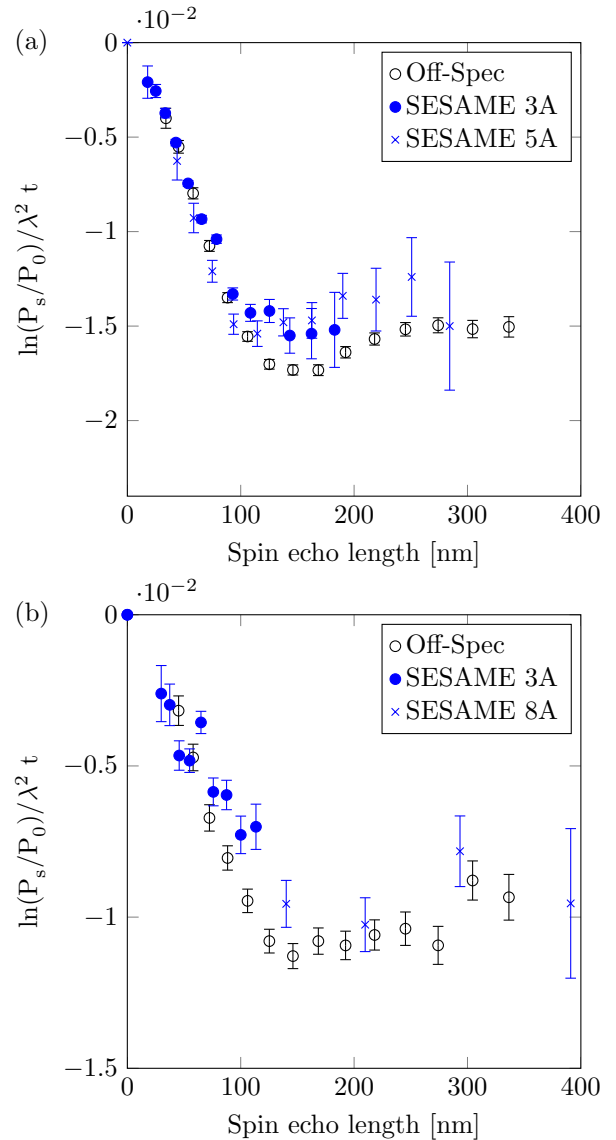

Figure 9. Silica stober particles (Radius 84nm) in H_2O (a) and H_2O and H_2O :D_2O (80:20)(b) measured on OffSpec and SESAME for two different Prism currents, as shown in the legend.

SILICA STÖBER PARTICLES

The Stöber method can be used to produce large volumes of monodisperse colloidal silica particles [43]. In order to evaluate the SESAME instrument for SESANS we prepared two samples which were measured ≈ 6 months apart on the SESAME instrument and at OffSpec at the ISIS pulsed neutron source.

Shown in figure 9 are measurements of the normalised SESANS signal for two different concentrations of silica Stöber particles in H_2O and H_2O :D_2O (80:20) on both SESAME and OffSpec. Two points are clear; the first is that at long spin-echo length ($G(z) \to 0$) the

values of the normalised SESANS signal, which are dependent upon the total (single) scattering cross section (Σ_t) agree within error. Also at short spin echo length the agreement is good. Especially considering the differences in spin-encoding methods, wavelength ranges, beam sizes and differences in analyser technology. Slight differences are observed in the measured G(z), these may be changes in the sample between measurements, however more statistics on the SESAME measurements are required to unambiguously answer these questions. The second point is the difference in statistical error. Data collection times for OffSpec and SESAME were ≈ 6 and 24 hours respectively. SESAME used a beam size of 200mm^2 and OffSpec 15^{2}mm. Errors in SESAME are a factor four larger than OffSpec. Accounting for differences in flux and beam size these differences agree within a factor of two with expectations based on the fluxes of the ISIS and LENS source.

DISCUSSION

The work described in this communication describes to our knowledge the first continuously pumped ^{3}He analyser used for SESANS, in fact to our knowledge this is the first use of continuous SEOP in any long term neutron scattering application, although nuclear physics have been using these devices for a number of years (for example [44]). The principle characteristics of the analyser are a larger acceptance angle than conventional super mirrors and also a uniform analysing power. For example supermirror channel polarisers may have strong positional dependence on both the transmission and polarisation characteristics [23]. Such behaviour would make the normalisation from the instrumental polarisation (P_0) invalid as the sample polarisation (P_s) would have a different spatial dependence. ^{3}He is one technology which does not have such a dependence. However the downside is the requirement of achieving a stable helium polarisation on the beam. This work shows that despite the additional equipment needed such a device is feasible to operate with a minimum of intervention.

The small $\approx 2\%$ variation in the ^{3}He polarisation renders the very short wavelengths unusable in our measurements, however it should be noted that by definition this is where G(Z) approaches unity and hence can be neglected in many cases. Alternatively measurements could be performed at short spin echo length with a lower field in the prisms.

The continuous pumping removes the need for time dependent corrections as the gas polarisation decays. It also keeps the polarisation high to make maximum use of the available neutron flux. Additional modifications could be performed to the ^{3}He analyser such as using a vertical magnetic field [45], which would have the added advantage of removing the need to have mirrors in the

beam and would allow the device to be placed closer to the sample, further increasing the angular acceptance. Also the angular acceptance can be further scaled up by the use of larger cells and/or narrower, higher-power lasers [46].

The coils used in this work have shown the importance of the interdigitation in resistive coils the efficacy of such interdigitation requiring careful fabrication and alignment of the coils. Any failure in the interdigitation results in a spatial variation in the flipping efficiency. Such a spatial variation renders the determination of the ratio P_s/P_0 inaccurate.

CONCLUSIONS

This paper has described the operation and performance of the first SESANS instrument with a continuously pumped ^{3}He spin analyser. The instrument is able to encode the neutron spin precession angle over a broad range of wavelengths and the encoding Wollaston prisms are well suited to a time-of-flight source.

The ^{3}He analyser has a large acceptance angle and allows large beams and samples to be used. The efficiency is uniform for all scattering angles to within 1% for wavelengths above 2.5 Å and hence normalisation to the instrumental polarisation (P_0) is valid for all scattering, unlike in the case of some supermirror polarisation analysers.

APPENDICES

A - Inaccuracies in G(z) arising from time dependence in the ^{3}He polarisation

For any SESANS measurement the quantity measured is given by;

$$P(z) = \exp(\Sigma_t[G(z) - 1]) \qquad (4)$$

where P(z) is the polarisation from the sample (P_s) normalised to the instrumental polarisation P_0. Therefore in any SESANS experiment variations in the ^{3}He polarisation will be convolved into the measurement of both P_0 and P_s. Inaccuracies in the determination of P(z) which will propagate through to inaccuracies in G(z). This inaccuracy can be mitigated by measuring both P_0 and P_s simultaneously, oscillating the measurements between the two by the use of an automated sample changer, or by using knowledge of the time dependence of the ^{3}He polarisation and applying corrections using similar methods to those suggested by Wildes [47]. However the simplest method is to minimise the fluctuations in the ^{3}He polarisation.

The total contribution of the derived polarisation,

P(z), for these time-dependent fluctuations is given by standard error calculation. The associated inaccuracies for various different fluctuations are shown in figure 10 as a function of neutron wavelength. At longer wavelength neutrons fluctuations in the ^3He polarisation have a minimal effect on the accurate determination of P(z), and hence G(z). Moreover the effect is only prevalent below 2.5Å, which is a region where both the neutron polarisation and flux are low.
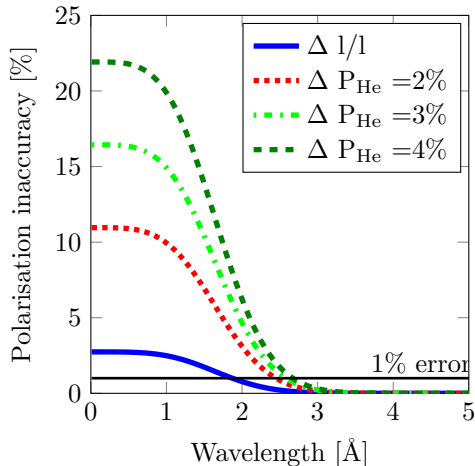

Figure 10. Calculated inaccuracies in P for variations in ^{3}He polarisation (Δ P_{He}) for the cell used in this work. Also the calculated error in the neutron polarisation arising from the difference in path length for the various different acceptance angles through the cell ($\Delta l/l$).

B - Stability algorithm for ^{3}He stability

Under steady state conditions the ^{3}He polarisation (P_{He}) is given by:

$$P_{He} = \frac{\gamma_{SE}}{\gamma_{SE} + \Gamma_{He}} P_{Rb} \qquad (5)$$

where Γ_{He} is the ^{3}He relaxation rate and γ_{SE} is the spin exchange rate. P_{Rb} is the Rb polarisation, given by:

$$P_{Rb} = \frac{\gamma_{opt}}{\gamma_{opt} + \Gamma_{SD}} \qquad (6)$$

where Γ_{SD} is the electron spin polarisation destruction rate, which is dependent upon the gas density and alkali metal used. γ_{opt} is the optical pumping rate given by:

$$\gamma_{opt} = \int I(\nu)\, \sigma(\nu)\, d\nu \qquad (7)$$

where $I(\nu)$ is the photon flux at frequency ν and $\sigma(\nu)$ is the photon absorption cross section for the Rb electron
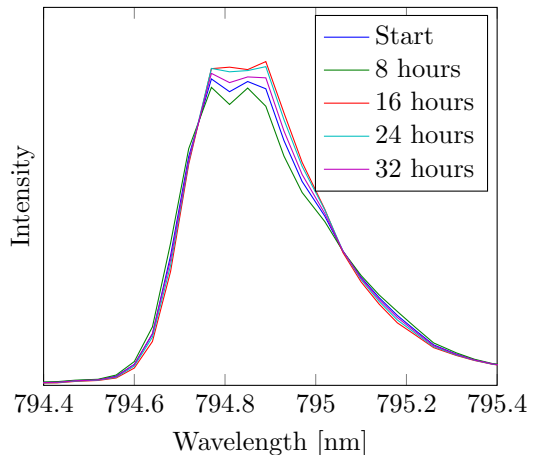

Figure 11. Selected laser spectra over the course of 32 hours as indicated in the legend.

transition. In order to achieve a stable ^3He polarisation then the alkali polarisation must be constant as the spin-echange and relaxation rates are constant in time. Hence the the laser spectral distribution ($I(\nu)$) must be constant ($\sigma(\nu)$) relative to the .

Figure 11 shows an off-line measurement of the laser spectrum. During the measurement the laser spectrum suffered from a fluctuating line shape, which causes the polarisation of Rb to be unstable in time , and eventually effects the polarisation of ^{3}He. To reduce the variation of ^{3}He polarisation, a feedback algorithm is added into the system. The idea is to tune the two small peaks either side of the D_1 absorption in Figure 11 to have equal height by adjusting laser current, so the absorption dip sits right on the Rb D_1 transition frequency, and Rb can get the most power from laser light. Figure 12 shows a comparison of the laser spectrum before and after applying the feedback algorithm. The Y axis is the ratio of the heights of the two peaks (tuned to be 1). It shows that the feedback changes the ratio of the peak more rapidly in time than without the feedback. The feedback sweeps the laser emission wavelength back and forth across the D_1 absorption and hence wastes some laser light. However as the ^{3}He polarisation/depolarisation rates are slow in comparison to the sweep rate of the laser this produces good stabilisation. More sophisticated feedback may be possible using a PID type algorithm. A further improvement may be to maximise the D_2 fluorescence (780nm [48]) to lock the laser wavelength.
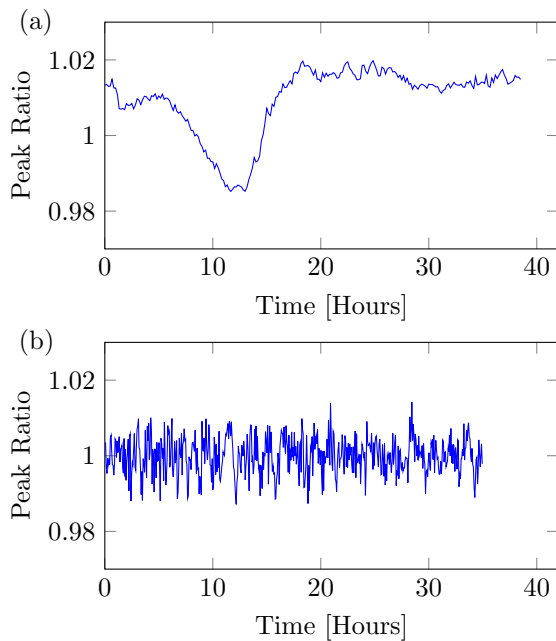
Figure 12. The ratio of the laser intensities on either side of the D_1 absorption line used in the algorithm to stabilise the laser wavelength. (a) is the ratio before applying the feedback algorithm, (b) is the ratio after applying feedback algorithm.

[1] R. Pynn, Neutron Spin Echo, edited by F. Mezei, Lecture Notes in Physics, Vol. 128, pp. 159–177. Heidelberg: Springer (1980).

[2] T. Keller, R. Gähler, H. Kunze, and R. Golub, Neutron News **6**, 16 (1995).

[3] M. T. Rekveldt, Nuclear Instruments and Methods in Physics Research Section B: Beam Interactions with Materials and Atoms **114**, 366 (1996).

[4] R. M. Dalgliesh, S. Langridge, J. Plomp, V. O. de Haan, and A. A. van Well, Physica B: Condensed Matter **406**, 2346 (2011).

[5] J. Plomp, V. O. de Haan, R. M. Dalgliesh, S. Langridge, and A. A. van Well, Thin Solid Films **515**, 5732 (2007).

[6] M. T. Rekveldt, J. Plomp, W. G. Bouwman, W. H. Kraan, S. Grigoriev, and M. Blaauw, Review of Scientific Instruments **76**, 033901 (2005).

[7] R. Pynn, M. Fitzsimmons, H. Fritzsche, M. Gierlings, J. Major, and A. Jason, Review of Scientific Instruments **76** (2005).

[8] M. Theo Rekveldt, Physica B: Condensed Matter **234–236**, 1135 (1997).

[9] M. T. Rekveldt, Journal of Applied Crystallography **36**, 1301 (2003).

[10] R. Ashkar, P. Stonaha, A. L. Washington, V. R. Shah, M. R. Fitzsimmons, B. Maranville, C. F. Majkrzak, W. T. Lee, W. L. Schaich, and R. Pynn, Journal of Applied Crystallography **43**, 455 (2010).

[11] D. V. Baxter, J. M. Cameron, V. P. Derenchuk, C. M. Lavelle, M. B. Leuschner, M. A. Lone, H. O. Meyer, T. Rinckel, and W. M. Snow, Nuclear Instruments and Methods B **241**, 209 (2005).

[12] C. M. Lavelle, D. V. Baxter, A. Bogdanov, V. P. Derenchuk, H. Kaiser, M. B. Leuschner, M. A. Lone, W. Lozowski, H. Nann, B. v. Przewoski, N. Remmes, T. Rinckel, Y. Shin, W. M. Snow, and P. E. Sokol, Nuclear Instruments and Methods in Physics Research Section A: Accelerators, Spectrometers, Detectors and Associated Equipment **587**, 324 (2008).

[13] T. Krouglov, W. G. Bouwman, J. Plomp, M. T. Rekveldt, G. J. Vroege, A. V. Petukhov, and D. M. E. Thies-Weesie, Journal of Applied Crystallography **36**, 1417 (2003).

[14] R. Andersson, L. F. Van Heijkamp, I. M. De Schepper, and W. G. Bouwman, Journal of Applied Crystallography **41**, 868 (2008).

[15] A. L. Washington, X. Li, A. B. Schofield, K. Hong, M. R. Fitzsimmons, R. Dalgliesh, and R. Pynn, Soft Matter **10**, 3016 (2014).

[16] R. Pynn, M. R. Fitzsimmons, W. T. Lee, V. R. Shah, A. L. Washington, P. Stonaha, and K. Littrell, Journal of Applied Crystallography **41**, 897 (2008).

[17] S. Parnell, H. Kaiser, A. Washington, F. Li, T. Wang, D. Baxter, and R. Pynn, Physics Procedia **42**, 125 (2013).

[18] S. R. Parnell, A. L. Washington, H. Kaiser, F. Li, T. Wang, W. A. Hamilton, D. V. Baxter, and R. Pynn, Nuclear Instruments and Methods in Physics Research Section A: Accelerators, Spectrometers, Detectors and Associated Equipment **722**, 20 (2013).

[19] P. Stonaha, J. Hendrie, W. T. Lee, and R. Pynn, Review of Scientific Instruments **84**, (2013).

[20] F. Li, S. R. Parnell, W. A. Hamilton, B. B. Maranville, T. Wang, R. Semerad, D. V. Baxter, J. T. Cremer, and R. Pynn, Review of Scientific Instruments **85**, (2014).

[21] R. Pynn, W. T. Lee, P. Stonaha, V. R. Shah, A. L. Washington, B. J. Kirby, C. F. Majkrzak, and B. B. Maranville, Rev Sci Instrum **79**, 063901 (2008).

[22] T. Walker and W. Happer, Rev. Mod. Phys. **69**, 629 (1997).

[23] X. Tong, J. Robertson, and R. Pynn, Nuclear Instruments and Methods in Physics Research Section A: Accelerators, Spectrometers, Detectors and Associated Equipment **768**, 77 (2014).

[24] G. L. Jones, J. Baker, W. C. Chen, B. Collett, J. A. Cowan, M. F. Dias, T. R. Gentile, C. Hoffmann, T. Koetzle, W. T. Lee, K. Littrell, M. Miller, A. Schultz, W. M. Snow, X. Tong, H. Yan, and A. Yue, Physica B: Condensed Matter **356**, 86 (2005).

[25] S. Boag, E. Babcock, K. Andersen, M. Becker, T. Charlton, W. Chen, R. Dalgliesh, S. Elmore, C. Frost, T. Gentile, R. L. Anton, S. Parnell, A. Petoukhov, M. Skoda, and T. Soldner, Physica B: Condensed Matter **404**, 2659 (2009).

[26] E. Babcock, S. Mattauch, and A. Ioffe, Nuclear Instruments and Methods in Physics Research Section A: Accelerators, Spectrometers, Detectors and Associated Equipment **625**, 43 (2011).

[27] R. Pynn, M. R. Fitzsimmons, H. Fritzsche, M. Gierlings, J. Major, and A. Jason, Review of Scientific Instruments **76**, 053902 (2005).

[28] R. Pynn, R. Ashkar, P. Stonaha, and A. L. Washington, Physica B: Condensed Matter **406**, 2350 (2011).

[29] W. C. Chen, T. R. Gentile, C. B. Fu, S. Watson, G. L. Jones, J. W. McIver, and D. R. Rich, Journal of Physics: Conference Series **294**, 012003 (2011).

[30] E. Babcock, B. Chann, T. G. Walker, W. C. Chen, and T. Gentile, Phys. Rev. Lett. **96**, 083003 (2006).

[31] W. C. Chen, R. Erwin, and S. M. Watson, Physics Procedia **42**, 163 (2013).

[32] M. V. Romalis and G. D. Cates, Physical Review A **58**, 3004 (1998).

[33] G. L. Jones, F. Dias, B. Collett, W. C. Chen, T. R. Gentile, P. M. B. Piccoli, M. E. Miller, A. J. Schultz, H. Yan, X. Tong, W. M. Snow, W. T. Lee, C. Hoffmann, and J. Thomison, Physica B: Condensed Matter **385–386, Part 2**, 1131 (2006).

[34] E. . Babcock, A. . Petoukhov, J. . Chastagnier, D. . Jullien, E. . Lelievre-Berna, K. . . H. . Andersen, R. . Georgii, S. . Masalovich, S. . Boag, C. . . D. . Frost, and S. . . R. . Parnell, Physica B: Condensed Matter **397**, 172 (2007).

[35] T. J. McKetterick, S. Boag, J. R. Stewart, C. D. Frost, M. W. A. Skoda, S. R. Parnell, and E. Babcock, Physica B: Condensed Matter **406**, 2436 (2011).

[36] S. R. Parnell, E. B. Woolley, S. Boag, and C. D. Frost, Meas. Sci. Technol **19**, 0 (2008).

[37] R. Jacob, J. Teter, B. Saam, W. C. Chen, and T. R. Gentile, Phys. Rev. A **69**, 021401(4) (2004).

[38] A. Stunault, K. H. Andersen, S. Roux, T. Bigault, K. Ben-Saidane, and H. M. Rønnow, *Proceedings of the Eighth International Conference on Neutron Scattering*, Physica B: Condensed Matter **385–386, Part 2**, 1152 (2006).

[39] S. Boag, S. Parnell, C. Frost, K. Andersen, and E. Babcock, Physica B **397**, 179 (2007).

[40] R. M. Dalgliesh, A. A. van Well, S. Boag, T. R. Charlton, C. D. Frost, V. O. de Haan, S. Parnell, and J. Plomp, Physica B: Condensed Matter **397**, 176 (2007).

[41] R. Pynn, M. R. Fitzsimmons, W. T. Lee, P. Stonaha, V. R. Shah, A. L. Washington, B. J. Kirby, C. F. Majkrzak, and B. B. Maranville, Physica B: Condensed Matter **404**, 2582 (2009).

[42] P. A. Seeger and L. L. Daemen, Nuclear Instruments and Methods in Physics Research Section A: Accelerators, Spectrometers, Detectors and Associated Equipment **457**, 338 (2001).

[43] W. Stöber, A. Fink, and E. Bohn, Journal of Colloid and Interface Science **26**, 62 (1968).

[44] C. E. Woodward, E. J. Beise, J. E. Belz, R. W. Carr, B. W. Filippone, W. B. Lorenzon, R. D. McKeown, B. Mueller, T. G. O'Neill, G. Dodson, K. Dow, M. Farkhondeh, S. Kowalski, K. Lee, N. Makins, R. Milner, A. Thompson, D. Tieger, J. van den Brand, A. Young, X. Yu, and J. Zumbro, Phys. Rev. Lett. **65**, 698 (1990).

[45] A. Petoukhov, V. Guillard, K. Andersen, E. Bourgeat-Lami, R. Chung, H. Humblot, D. Jullien, E. Lelievre-Berna, T. Soldner, F. Tasset, and M. Thomas, Nucl. Instr. And Meth. In Phys. Res. A **560**, 480 (2006).

[46] W. C. Chen, T. R. Gentile, Q. Ye, T. G. Walker, and E. Babcock, Journal of Applied Physics **116**, (2014).

[47] A. R. Wildes, Neutron News **17**, 17 (2006).

[48] W. Happer, Rev. Mod. Phys. **44**, 169 (1972).